Te-hyperdoped silicon layers for visible-to-infrared photodiodes

© F.F. Komarov,[1,2] S.B. Lastovsky,[3] I.A. Romanov,[4] I.N. Parkhomenko,[4] L.A. Vlasukova,[4] G.D. Ivlev,[4]
Y. Berencen,[5] A.A. Tsivako,[6] N.S. Kovalchuk,[6] E. Wendler[7]

[1]A.N. Sevchenko Institute of Applied Phisics Problems of Belarusian State University,
220045 Minsk, Republic of Belarus
[2]National University of Science and Technology „MISiS",
119049 Moscow, Russia
[3]Scientific and Practical Materials Research Center, National Academy of Sciences of Belarus,
220072 Minsk, Republic of Belarus
[4]Belarusian State University,
220030 Minsk, Republic of Belarus
[5]Helmholtz-Zentrum Dresden-Rossendorf (HZDR) Institute of Ion Beam Physics and Materials Research,
01328 Dresden, Germany
[6]JSC Integral,
220108 Minsk, Republic of Belarus
[7]Institute for Solid State Physics, Friedrich-Schiller-University Jena,
07743 Jena, Germany
e-mail: komarovf@bsu.by

Silicon layers doped with tellurium up to concentration $(3-5) \cdot 10^{20}\,\text{cm}^{-3}$ have been formed by ion implantation with subsequent pulsed laser annealing. It was shown that $70-90\%$ of the introduced impurity is in the substitution position in the silicon lattice. Te hyperdoped silicon layers exhibit significant absorption $(35-65\%)$ both in the visible and near IR $(1100-2500\,\text{nm})$ spectral ranges, and the absorption increases with increasing wavelength. The current-voltage and capacitance-voltage characteristics, as well as the photosensitivity of photodetectors based on Te-doped silicon layers have been presented and discussed. The residual structural defects in implanted Si layers have been investigated by deep-level transient spectroscopy.

Keywords: silicon, hyperdoping, tellurium implantation, laser annealing, impurity subband, deep-level transient spectroscopy.

Introduction

Silicon is the main semiconductor material used to manufacture integrated circuits and it dominates the market with a share of around 90%. Ultra-highly integrated silicon chips form the backbone of modern microelectronics and enable exponential growth in computing performance. The performance of integrated circuits (microprocessors, graphics chips, RAM chips, etc.) is determined by the switching speed of the MOS-transistor components and the speed of data exchange. Over the last three decades, the speed of active elements on a silicon crystal has doubled every one and a half to two years (Moore's Law), while the speed of carriers in the metal conductors connecting the individual components of an integrated circuit has remained constant. While the performance of early processors was mainly determined by the transistors speed, nowadays, the interconnect contribution to the total delay on logic elements is comparable to, or even exceeds, the switching times of the transistors. Thus, it is the connection and information exchange time between the constituent elements that determines the performance

limit of „traditional" microprocessors. The most promising solution to increasing the speed of future integrated circuits is optical data transmission within the Si-crystal. Optical interconnects provide data rates of $\sim 30-60$ Gbps, the limit of copper technology is estimated to be 20 Gbps [1,2]. In addition, optoelectronic devices consume considerably less power. In recent years, microelectronics and opto-electronics specialists have been working hard to develop high performance emitters and receivers in the visible (~ 0.3 to ~ 0.8m), near infrared (NIR) (~ 0.8 to $\sim 2\,\mu\text{m}$) and mid-IR (~ 2 to $\sim 25\,\mu\text{m}$) regions, silicon waveguides and modulators whose fabrication will allow electronic and optical devices to be integrated in a single integrated circuit [1–4]. In integrated silicon photonics devices, detectors must detect photons with energies less than the band gap width of Si ($E_g = 1.12$ eV or with wavelengths greater than $1.1\,\mu\text{m}$) that can propagate efficiently with minimum loss within a fiber or other waveguide medium. Existing silicon photodetectors are insensitive to the three main bands of fiber optic telecommunications systems: S $(1460-1530)$, C $(1530-1565)$ and L $(1565-1625)$ nm [5].

In recent years, various strategies have been developed and tested for near- and mid-infrared silicon photodetectors with effective photosensitivity. These include the development of photodetectors based on Si−Ge [4] Group 4 heterostructures and creation of photosensitive layers by modifying the band structure and generation of intermediate states in the band gap of Si through irradiation with Si^+, Ar^+ ions, protons or neutrons [6,7]. In the first mentioned approach, due to the lattice parameter mismatch of 4.2% between Si and Ge layers, the epitaxial Ge layers formed had a high density of penetrating dislocations and high surface roughness, which prevents the integration of such Ge layers in CMOS silicon planar technology. In the second approach, radiation-formed silicon layers are capable of generating current carriers at the expense of $\hbar\omega < E_g^{Si}$ quanta, but the absorption coefficient of such layers was very low ($\alpha \approx 0.5-50 \, cm^{-1}$) [6].

An alternative is to introduce states into the forbidden zone by alloying Si with conventional p- and n-type impurities, i.e. groups III (B, Al and Ga) and V (P, As and Sb), which provides absorption of [8,9] IR quanta. Si-photodetectors based on small alloying impurities exhibit broadband photosensitivity but operate at temperatures below 40 K due to intense thermal generation of free carriers at higher temperatures [10]. As a result, the thermo-ionization of the carriers affects the ratio of the optical generation output to their thermo-generation, which precludes the use of such photodetectors at room temperature.

A number of the world's leading micro- and optoelectronic laboratories have developed and researched photodetectors by implementing the principles of creating impurity subbands in the Si band gap by introducing impurities that create deep levels with ionization energies of hundreds of meV [11,12]. These near- and mid-IR photodetectors can effectively operate at room temperatures. It should be noted that the equilibrium solubility limit of impurities creating deep levels in silicon is $\sim 10^{16} \, cm^{-3}$ [13], which is several orders of magnitude lower than this value for small alloying impurities (over $10^{19} \, cm^{-3}$) [13]. Importantly, to form an impurity subzone in the silicon band gap, the concentration of the dopant impurity must exceed $10^{18} \, cm^{-3}$ [14]. This indicates that non-equilibrium heat treatment methods are required to produce such high alloying levels. It should be noted that there is another obstacle to realizing high concentrations of such impurities: their high diffusive mobility in Si. In contrast to fine alloying impurities, the diffusion coefficients of deep level impurities appear to be many orders of magnitude higher [15]. This suggests that long heat treatment processes are unacceptable.

By now, it has been established that the highest absorption coefficient of light in the IR range (up to $\sim 3 \, \mu m$) at room temperature ($\sim 10^4 \, cm^{-1}$ is observed in monocrystalline silicon oversaturated with chalcogen atoms (S, Se, Te) [16].

The equilibrium solubility of chalcogenes in silicon is also $\sim 10^{16} \, cm^{-3}$. At these concentrations, chalcogenes create deep levels in the band gap of silicon. However, when the equilibrium solubility is exceeded by 4−5 orders of magnitude, the impurity levels merge into a subzone. It becomes possible to absorb photons through the electronic transitions „valence band−impurity subzone" and „impurity subzone−conduction band" [17]. To achieve hypersaturation, chalcogen alloying of silicon is done using non-equilibrium techniques such as ion implantation followed by femto-, pico-, nanosecond laser [16,18,19] or flash annealing [20].

The present work is devoted to the creation of hypersaturated tellurium layers of Si using ion implantation and pulsed laser annealing. The research focuses on determining the effect of pulsed laser annealing (PLA) regimes on the structural, optical and electrophysical properties of the alloyed layers. Test photodiode structures were made and their volt-ampere and voltage-capacitance characteristics were measured. The photosensitivity of the structures formed under different PLA modes to visible and near-IR range as well as the effect of subsequent low-temperature treatment (400°C) on the volt-ampere characteristics (VAC) have been evaluated.

1. Materials and research techniques

Si (111) p-type conductivity substrates with resistivity $\rho = 10 \, \Omega \cdot cm$, polished on both sides were implanted with Te^+ ions at 200 keV energy with a fluence of $1 \cdot 10^{16} \, cm^{-2}$. Then pulsed laser annealing with a ruby laser ($\lambda = 694 \, nm$, annealing duration $\sim 70 \, ns$ at 0.5 level with a uniform pulse energy distribution over a 4×4 mm PLA zone) was performed. The energy density W in the laser pulse (PLA zone) was set to 1.5, 2 and 2.5 J/cm^2. In some cases, additional low-temperature annealing of samples (400°C, 15 min) in an argon stream (200 sccm) was used.

The analysis of the interstitial impurity depth distribution, the share of tellurium atoms in the silicon lattice nodes and the degree of crystallinity of the implanted layers were performed by recording Rutherford backscattering spectra of He^+ ions with 1.5 MeV energy in the channeling mode (RBS/Ch) along the „100" and without it. RBS simulation spectra using the SIMNRA [21] software was performed in steps until a full match with the experimental spectra. To investigate the optical properties, Raman spectra (RS), transmittance (T) and reflection (R) were taken. RS spectra were recorded in backscattering geometry on a Ramanor U1000 micro-Raman spectrometer (Jobin Yvon) under excitation by a 532 nm laser. Transmission and reflection spectra were taken on a Lambda 1050 WB spectrophotometer (PerkinElmer) in the range of 200−2500 nm. The absorption spectrum (A) was calculated using the formula

$$A = 100\% - R - T.$$

The VAC was measured using an IPPP1/6 semiconductor parameter meter at measurement temperatures of $T_{reg} = 290$ and 80 K. Characteristics were measured with and without illumination (dark). The distribution of charge

carrier concentration $N(x)$ in the less doped region of the investigated structures was determined from the analysis of the voltage-capacitance $(C-U)$ dependences. This method is based on recording the capacitance values of a sharply asymmetric $p-n$-junction as the reverse bias voltage U_{rev} changes. The barrier capacitance of n^+-p-structures was measured at $T_{reg} = 290$ and 80 K at 1 MHz using an LCR E7-17 meter.

The residual defects in the structure (emission activation energy and charge carrier capture cross-section) were characterized by non-stationary Deep Level Transient Spectroscopy — DLTS) [22]. The measurement was carried out with a capacitive spectrometer based on a high-frequency full conductivity bridge with automatic capacitance balancing. In addition, the set of equipment consisted of a PC-based recording and control system, a temperature control unit and a nitrogen cryostat.

2. Results and discussion

2.1. Structure and elemental composition

Fig. 1 shows the RBS/Ch spectra. As can be seen from the figure, PLA causes a diffusive redistribution of the impurity both deep into the sample and towards the surface.

Fig. 2 shows the concentration profiles of the impurity distribution obtained by simulation in the SIMNRA software until the experimental and simulated spectra coincide completely. The concentration profile of the embedded impurity, calculated using BEAM2HD [23], is also shown. It should be noted that there is good quantitative agreement between the theory and experimental data, both in terms of the position of the concentration maximum and the value of the concentration as a function of depth over
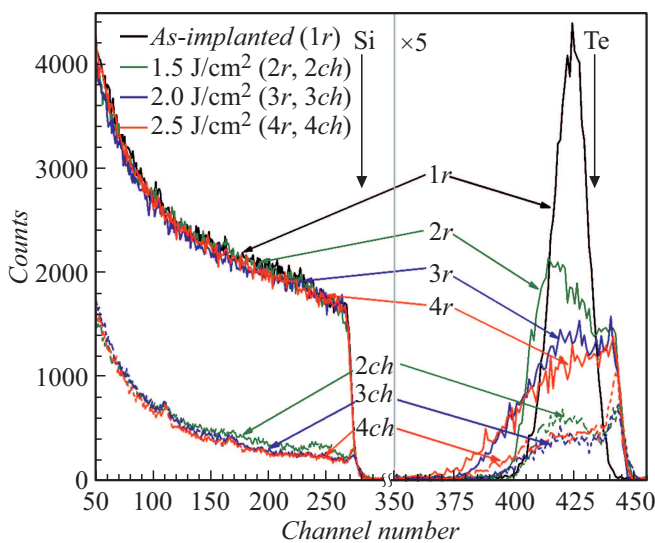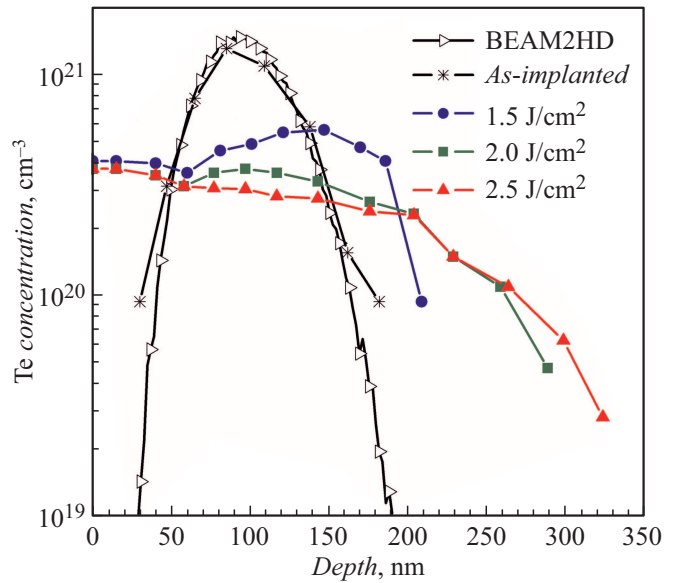

Figure 2. Modelled tellurium atom concentration profile and experimental tellurium atom concentration profiles for an implanted Si sample without annealing and for different heat treatment modes.

the entire range of concentrations recorded by the RBS. Immediately after implantation, the tellurium concentration at a maximum depth of ~ 80 nm is $\sim 1 \cdot 10^{21}$ cm^{-3}. After laser treatment at $W = 1.5$ J/cm^2, a concentration plateau is formed in the depth region from the surface to 190 nm, in the region where the tellurium concentration reaches $(4-5) \cdot 10^{20}$ cm^{-3}. At laser pulse energy densities of 2.0 and 2.5 J/cm^2 the tellurium concentration in plateau region decreases to $3 \cdot 10^{20}$ cm^{-3} due to diffusion of some impurity deep into the sample to depths of 300 and 330 nm after PLA with $W = 2.0$ and 2.5 J/cm^2, respectively. The integral number of implanted impurity atoms determined from the distributions of atomic concentrations over the depth of silicon shown in Fig. 2, is $1 \cdot 10^{16}$ cm^{-2} for the as-implanted sample and for the sample after PLA with energy density $W = 1.5$ J/cm^2, $0.9 \cdot 10^{16}$ cm^{-2} and $0.8 \cdot 10^{16}$ cm^{-2} for annealing with $W = 2.0$ J/cm^2 and $W = 2.5$ J/cm^2, respectively. Considering the accuracy of the ion fluence measurement during implantation and analysis of the concentration profiles (sensitivity of RBS method ~ 0.01 at.%), a weak influence of the PLA mode on the total impurity content with a tendency to its decrease with increasing laser pulse energy density can be noted.

RBS spectra taken in channeling mode indicate that the tellurium-implanted Si layer without PLA is in an amorphous state. The thickness of the Si amorphous layer after Te$^+$ ion implantation with fluence of $1 \cdot 10^{16}$ cm^{-2} without PLA, obtained from the RBS/Ch of spectrum for this sample (not given), is $\sim 0.2 \mu$m. The values χ^{Si} and χ^{Te}, which show the integral ratios of the channeled to undirected spectrum samples in the Si and Te related channels respectively, are used to estimate the degree of Si crystallinity and Te share of substitution positions in the

Figure 1. RBS/Ch spectra of Si samples, hyper-saturated Te: *1* — original, *2−4* — after annealing: *2* — 1.5, *3* — 2, *4* — 2.5 J/cm^2. The *1r−4r* spectra are taken in „random"mode, the *2ch−4ch* spectra are taken in channeling mode.

Table 1. The values of χ^{Si} and f for Si samples, hyper-saturated with Te

| Parameter/sample	$W=1.5\,\mathrm{J/cm^2}$	$W=2.0\,\mathrm{J/cm^2}$	$W=2.5\,\mathrm{J/cm^2}$
$\chi^{Si}, \%$	23.9	23.1	21.2
$f, \%$	91.2	90.4	73.6

Si lattice. The impurity atom fraction in the silicon lattice nodes f was calculated using the formula in [24]:

$$f = (1-\chi^{Te})/(1-\chi^{Si}).$$

The values of χ^{Si} and f are presented in Table 1.

As shown in Table 1, the value range of χ^{Si} of silicon hyper-saturated with tellurium after PLA is $23.9-21.2\%$, with χ^{Si} decreasing with increasing energy density in the pulse. By comparison, in a perfect single crystal $\chi^{Si} \le 5\%$ and in a completely amorphous material $\chi^{Si} = 100\%$ [24]. Thus, the degree of crystallinity of the hyper-saturated tellurium silicon is maximum after laser annealing with maximum energy density $W = 2.5\,\mathrm{J/cm^2}$. The residual structure damage after recrystallisation of amorphous silicon layers, as well as some tellurium atoms that do not enter the Si lattice nodes and form atomic clusters, cause an increased yield in the channeled RBS spectra. The effective functioning of the silicon photodetector is ensured under the condition of structural perfection of the doped layer and high activation degree of the introduced impurity [16,18–20]. Analysis of RBS spectra in channeling mode indicates that laser annealing also causes Te atoms to enter silicon lattice nodes, and the degree of impurity activation is very high at $(73.6-91.2\%)$. The lower the PLA energy, the more impurities end up in the substitution positions in the silicon lattice.

Fig. 3 shows the RS spectra of the implanted silicon samples before and after heat treatment. The spectrum of the original silicon wafer is characterized by a narrow symmetrical band with a maximum at $520\ \mathrm{cm^{-1}}$ due to optical phonon scattering. After implantation, this band disappears, indicating complete amorphization of the implanted silicon layer. After PLA, the band is recorded again, indicating that the crystalline structure of the doped silicon layer has been restored. For a sample irradiated by a laser pulse with $W = 1.5\,\mathrm{J/cm^2}$, a signal from the silicon matrix is also recorded, and the RS spectrum in the spectral region discussed can be approximated by two bands: a weak band with a maximum at $511\,\mathrm{cm^{-1}}$ and a more intense one at $519.7\,\mathrm{cm^{-1}}$. The appearance of these bands indicates the presence of two recrystallized layers with different levels of residual stress. This may be due to the different recrystallisation rates of silicon layers with different levels of alloying impurities. Increasing the energy in the pulse (up to $2-2.5\,\mathrm{J/cm^2}$) results in a shift of the low-frequency band towards higher frequencies. Thus, with increasing energy in the pulse, the degree of structural
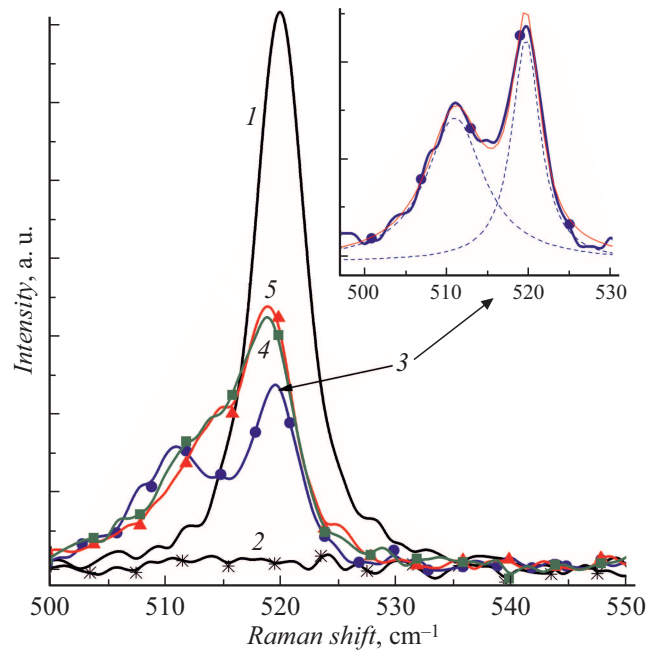
Figure 3. Raman spectra of original silicon wafer (*1*) silicon implanted with Te before (*2*) and after laser annealing with energy density pulses 1.5 (*3*), 2 (*4*), 2.5 (*5*) J/cm².

perfection of the recrystallized layer of implanted silicon increases, but the structure is not completely restored. The RS data are consistent with the RBS/Ch results (Table 1). It is known that the molten layer thickness and liquid phase existence time [25,26] increase with increasing energy density of nanosecond PLA. This is the reason for the different degrees of structural perfection of the alloyed layer in our case.

2.2. Optical properties

Fig. 4 shows the absorption spectra of the implanted samples in the wavelength range $200-2500\,\mathrm{nm}$.

As can be seen, for the sample immediately after implantation (,,Si + Te"), a decrease in the absorption coefficient in the visible region and an increase of $1-6\%$ in the $1100-2000\,\mathrm{nm}$ region is observed. This effect is presumably caused by the absorption of IR photons on radiation defects. At the same time, in the implanted samples after PLA, an intense light absorption with an energy lower than the band gap width of silicon is observed. For a sample after laser annealing with $W = 1.5\,\mathrm{J/cm^2}$ the absorption coefficient increases from 34% at $\lambda = 1180\,\mathrm{nm}$ to 55% at $\lambda = 2500\,\mathrm{nm}$. The effect of increasing absorption coefficient with wavelength for samples after PLA with $W = 2.0$ and $2.5\,\mathrm{J/cm^2}$ is even more pronounced. In this case, the absorption coefficient increases from 35% at $\lambda = 1180\,\mathrm{nm}$ to 64% and 65%, respectively, at $\lambda = 2500\,\mathrm{nm}$.

Absorption in the visible and IR ranges can be increased by tens of per cent by depositing a thin layer of SiO_2 on the surface of the formed structure by suppressing the reflection
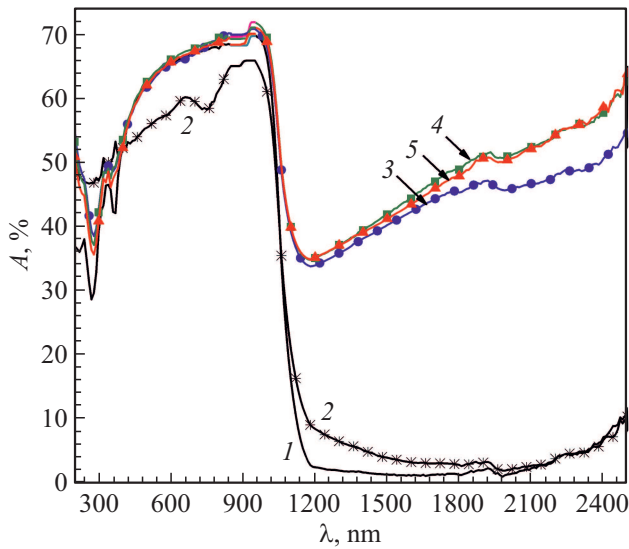
Figure 4. Absorption spectra of original silicon wafer (*1*) silicon implanted with Te before (*2*) and after laser annealing with energy density pulses 1.5 (*3*), 2 (*4*), 2.5 (*5*) J/cm^2.

coefficient of the radiation. The light reflection coefficient of the SiO$_2$ layer at $T = 300$,K is much lower than that of silicon and is $0.05-0.1$ and the light absorption coefficient α of the SiO$_2$ layer is $\sim 0.01\alpha_{Si}$ [26]. Disturbed and amorphized Si layers do not exhibit strong absorption near the fundamental absorption edge, and the absorption coefficient decreases rapidly with increasing wavelength [27]. Consequently, the high absorption of the implanted layers after PLA can only be due to the high concentration of Te atoms in the substitution positions in the Si lattice and the formation of an impurity subzone inside the silicon band gap E_g^{Si}.

The chalcogen atoms (Te, Se) in the Si lattice are double donors. The introduction of low concentrations of Te atoms corresponds to the appearance of deep donor states in the upper half of E_g^{Si} [28]: E_C — 0.199 eV and E_C — 0.411 eV, counting from the bottom of the conduction zone E_C. At high donor concentrations, their wave functions overlap, leading to a broadening of the donor levels and the formation of an impurity subzone. With a further increase in the concentration of the doping impurity, the width of the impurity subzone increases until it overlaps with the conductive zone. As a subzone rough estimate, the threshold concentration of replacement Te atoms in the Si lattice to provide an insulator−metal transition, calculated from Mott's theory [29], is $\sim 2.65 \cdot 10^{20}$ cm^{-3} [30]. According to Table 1 and Fig. 2, the average concentration of substituted Te atoms in Si layer of thickness 0.20μm for the PLA-treated samples is $3.6 \cdot 10^{20}$, $3.1 \cdot 10^{20}$ and $2.2 \cdot 10^{20}$ cm^{-3} for PLA with $W = 1.5$; 2.0 and 2.5 J/cm^2, respectively. The width of the extrinsic subzone ΔE_{IB} according to [31] is defined as

$$\Delta E_{IB} = \frac{e^2 N_d^{1/3}}{4\pi\varepsilon_0\varepsilon_r}, \qquad (1)$$

where e — electron charge, ε — vacuum permittivity, ε_r — high frequency Si permittivity, N_d — donor concentration.

According to (1) and the above data for N_d in the three PLA modes, we obtain that ΔE_{IB} varies from 0.11 eV for $W = 1.5$ Jcm^2 to 0.07 eV for $W = 2.5$ Jcm^2. In the framework of more rigorous calculations based on density functional theory [32] for silicon with close level of tellurium doping: 1 tellurium atom per 215 silicon atoms, corresponding to $2.33 \cdot 10^{20}$ at./cm^3, the width of the impurity subzone is 0.25 eV. This zone is located 0.47 eV away from the valence band $\Delta E(VB - IB)$ and 0.38 eV away from the conduction zone of silicon $\Delta E(IB - CB)$.

2.3. Photovoltaic characteristics

The hyper-saturated tellurium layers of silicon have been used to make photodiodes. A structural scheme of the devices is shown in Fig. 5. The top ring-shaped nickel electrodes were created by magnetron sputtering of the target. This process was accompanied by photolithography and plasma-chemical silicon etching operations in SF6 to a depth of 2μm to form mesostructures. As bottom electrodes, Al layers about 200 nm thick were deposited.

2.3.1. VAC of photodiodes
In the direct VAC measurement, the negative electrode was connected to the nickel contact and the positive one — to the substrate of the structure. When measuring the reverse VAC —, vice versa. Fig. 6, *a, b* shows the dark and illuminated VAC of the sample after Te$^+$ ion implantation without heat treatment at $T_{reg} = 290$ and 80 K. The value of the direct offset on the structure increased to $U_{forw} = 3$ V. In this case, the maximum current was 1.5 mA at 290 K (Fig. 6, *a*) and 0.02 mA at 80 K (Fig. 6, *b*). The inverse VAC were measured up to $U = -10$ V. At $T_{reg} = 290$ K illumination has almost no effect on the forward and reverse branches. The maximum reverse current was $9 \cdot 10^{-5}$ A. These data indicate that the mechanism of thermally activated carrier injection at this temperature is the dominant one. Measurement at $T_{reg} = 80$ K revealed a strong suppression of this injection mechanism (Fig. 6, *b*). At a measuring temperature of 80 K, the value of the dark reverse current decreases by six orders of magnitude. In the bias voltage range U_{rev} from -4 to -10,V illumination increases reverse currents by a factor of
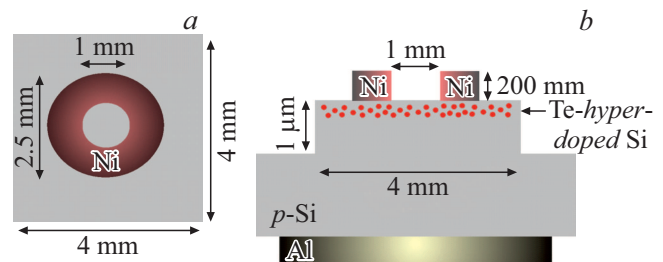

Figure 5. Schematic of the photodiode test structure: *a* — top view, *b* — test photodiode structure with a tellurium hyperdoped silicon layer.
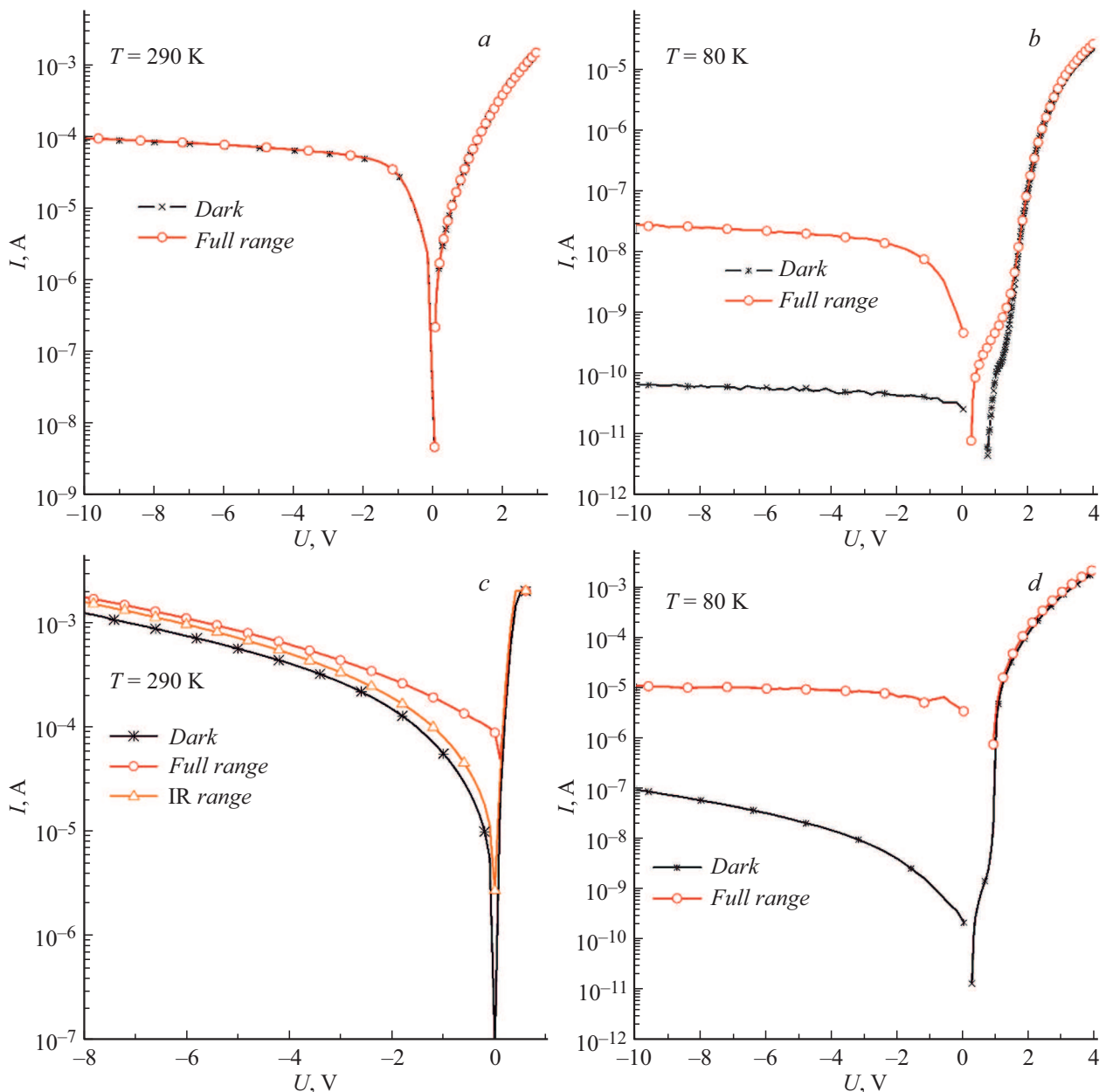
Figure 6. The forward and reverse VAC of Te-implanted silicon before (a, b) and after laser annealing (c, d) pulse with $W = 2 \, \text{J/cm}^2$, measured without and with illumination at $T_{reg} = 290 \, \text{K}$ (a, c) and $80 \, \text{K}$ (b, d).

about 300. In addition, illumination of the sample leads to an increase in forward current in the initial region of the VAC.

Considering that after implantation of Te^+ ions an amorphous silicon layer $(\sim 0.2 \, \mu\text{m})$ is formed, heat treatment at $400°C$ for $15 \, \text{min}$ in an argon atmosphere was carried out to stabilize the structural state of this layer. The VAC of the formed structure were measured at $290 \, \text{K}$ with halogen illumination $(\sim 3000 \, \text{K})$ in the full luminescence range (Full Range) and with silicon illumination (IR Range), the photosensitivity of the IR range structure was determined (Fig. 7). When changing to Full Range mode, the distance from the source to the instrumentation structure was chosen

to ensure that it is not heated. Fig. 7 shows that heat treatment at $400°C$ results in a photosensitive sample at the measuring temperature of $290 \, \text{K}$. The maximum value of the illumination current ratio (I_L) to the dark current (I_D) is $I_L/I_D = 17$ and is reached at negative bias $U_{rev} = -2 \, \text{V}$. Illuminating the sample in the IR increases the reverse current by a factor of 4 when the bias voltage U_{rev} ranges from -1.5 to $-2 \, \text{V}$.

PLA samples at different laser energies result in a photocurrent at zero bias and halogen lamp illumination over the entire range. The photovoltaic EMF of the resulting structures is $0.1-0.2 \, \text{V}$. The post-PLA VAC structures with energy $2 \, \text{J/cm}^2$ measured at 290 and $80 \, \text{K}$ are shown in

Table 2. Dark current values and relative photo-conversion efficiencies of photodetectors formed under different heat treatment regimes

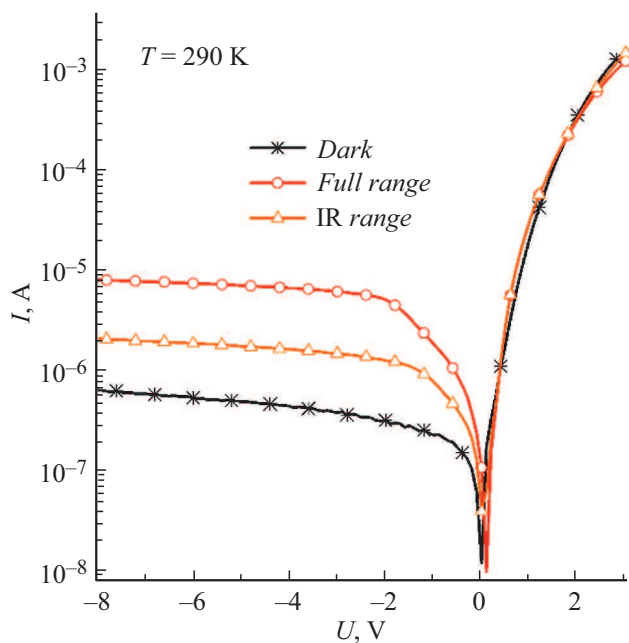| T_{reg}, K	Dark energy the laser pulse, J/cm^2	I_{forw}^{max}, mA	I_{rev} density at $U_{rev} = -10$ V, mA	I_L/I_D at $U_{rev} = -10$ V, a.u.
290	0	1.5	$9 \cdot 10^{-2}$	~ 1
	1.5	63.5	1.2	~ 1.5
	2	75	1.6	~ 1.3
	2.5	100	1.2	~ 1.4
80	0	2	$8 \cdot 10^{-8}$	300
	1.5	2	$3 \cdot 10^{-5}$	1200
	2	2.1	$9 \cdot 10^{-5}$	1000
	2.5	1.7	10^{-3}	95

Figure 7. Te-implanted silicon VAC after heat treatment at 400°C, measured without and with illumination at $T_{reg} = 290$ K.

Fig. 6, *c, d*. Shading the sample at room temperature slightly increases the current of the reverse branch of the VAC and has almost no effect on the change in current of the forward branch of the VAC when the voltage U_{forw} exceeds 0.2 V. The ratio I_L/I_D, increases rapidly as the reverse bias voltage increases from -10 to 0 V. The dark current of the photodiode structure measured at 80 K is 4 orders of magnitude lower than the dark current measured at room temperature (Fig. 6, *d*). Lighting the sample with a halogen lamp at low temperature increases the reverse branch current by $2-3$ orders of magnitude in the voltage range U_{rev} from -0.5 to -10 V. The post-PLA VAC structures at different energies have a similar appearance. Table 2 shows the forward current values measured at voltage $U_{forw} = 4$ V,

the dark current and the ratio I_L/I_D for the photodiode structures at temperatures of 290 and 80 K.

The values I_L/I_D are obtained with a bias voltage of -10 V and illumination by a halogen lamp over the full range. Table 2 shows that the dark current of the structure fabricated after PLA with energy 2.5 J/cm^2 is significantly higher than that of samples annealed by laser pulse with energies 1.5 and 2 J/cm^2. The ratio of photocurrent to dark current obtained at room temperature is weakly dependent on irradiation energy and is in the range of $1.3-1.5$. On the other hand, the photo-conversion efficiency measured at 80 K significantly depends on the irradiation energy and decreases rapidly from 1200 to 95 when the laser pulse energy increases from 1.5 to 2.5 J/cm^2. This dependence can be explained by the presence of defects with different activation energies, the concentration of which depends on the laser annealing energy. The sample annealed at $W = 1.5$ J/cm^2 has the highest photo-conversion efficiency, measured at temperatures of 290 and 80 K and a bias voltage of -10 V.

Particularly noteworthy are the effects due to additional heat annealing at 400°C for 15 min. Since the step of the VAC measurement was 0.2 V, the maximum photo-conversion efficiency (parameter I_L/I_D) was calculated at bias voltage $U_{rev} = -0.2$ V. Table 3 shows the maximum values of I_L/I_D measured before and after heat treatment of samples at 400°C. The highest photo-conversion efficiency in the IR range before and after heat treatment as well as in the visible range before the heat treatment is obtained for the sample which underwent PLA with $W = 2$ J/cm^2. The results of the above discussed structural and optical properties of the formed layers indicate discussed that both the good structural perfection of the layer and the high percentage of the substitutional tellurium fraction in the silicon lattice correspond to this PLA energy density. Heat treatment resulted in an increase of I_L/I_D when illuminated by a halogen lamp throughout the range. On the other hand, the heat treatment had almost no effect on the photo-conversion intensity of the IR illumination.

In general, such heat treatments after PLA can improve the crystallinity quality of the doped layer, increase the electrical activation level of the introduced impurity and the absorption in the IR range due to the breakdown and activation of tellurium complexes formed during the PLA process. Undoubtedly, more research is needed to improve the efficiency of photodetectors in the visible and infrared regions. This can be achieved by a special design of the upper and lower electrodes to enhance the collection efficiency of the light-generated carrier, and by the use of an anti-reflective coating. In addition, passivation of the top side or both of the structure (a thin layer of SiO_2 or Si_3N_4), and the use of a point contact on the back side of the detector will significantly suppress surface carrier recombination. Diode performance and photosensitivity strongly depend on fabrication conditions, including type and level of substrate and implanted layer doping, PLA parameters and final equilibrium heat treatment regimes. In order to maximize the use of light-generated carriers at room temperature, the intermediate subzone created by the hyper-doping chalcogenes must be isolated by an adequate gap from both the conduction and valence bands. The development of a horizontal (planar) structure for such photodetectors is also of interest for the efficient collection of current carriers.

2.3.2. Voltage-capacitance characteristics

From capacitive measurements at different voltages and temperatures of 290 and 80 K, the concentration of charge carriers $N(x)$ in the less doped region of the investigated structures and the width of the spatial charge region (SCR) were determined. Fig. 8, a shows the $C-U$-characteristics of the structure without PLA, measured at 290 and 80 K. Capacitance values at zero bias are $30-33$ pF and are only weakly dependent on temperature. At both temperatures, the dependence $C(U)$ has a non-monotone form, which is most pronounced at $T = 290$ K. Such an unusual $C-U$-characteristic was obtained in [33] for a silicon diode containing a δ-layer of point three-charged defects in a symmetrical $p-n$-transition.

Fig. 8, b shows the distribution of charge carrier concentration $N(x)$ in the less doped region of this structure. The $N(x)$ dependences were determined assuming a sharply asymmetric $p-n$-transition from the $C-U$-characteristics shown in Fig. 8, a. The large width of the spatial charge region (SCR) ($\approx 6.5\,\mu$m) at zero displacement on the sample and the somewhat unusual „falling" appearance of the $N(x)$ dependences are noteworthy. The width of the SCR increases as the value of E_g increases (see below, expression (2)). The case of amorphous silicon corresponds to a band gap width of $E_g \approx 1.7-1.8$ eV. With decreasing temperature the width of the SCR increases twofold, which may indicate a high concentration of radiation defects in this region of the structure after implantation of Te^+ ions, as well as a decrease in the concentration of mobile carriers $N(T)$ at low T (see (2)). It should be noted that systems
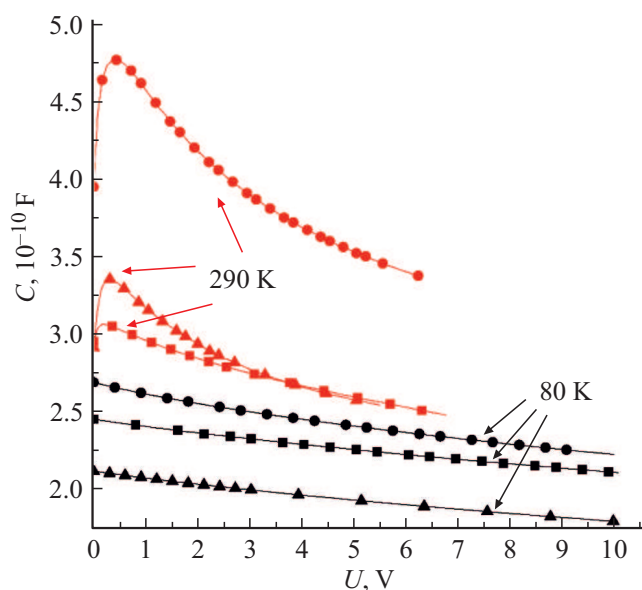

Figure 8. $C-U$-characteristics of Te-implanted silicon after laser annealing pulse with $W = 1.5$ J/cm^2 (▲), $W = 2$ J/cm^2 (■) and $W = 2.5$ J/cm^2 (●), measured at $T_{reg} = 290$ and 80 K.

with a large width of the SCR are characterized by a higher probability of registration of low-energy quanta due to the increased probability of absorption of such quanta, generation and separation of current carriers of different sign in this region [34]. Only the quanta absorbed in the SCR contribute to the photo-generation current.
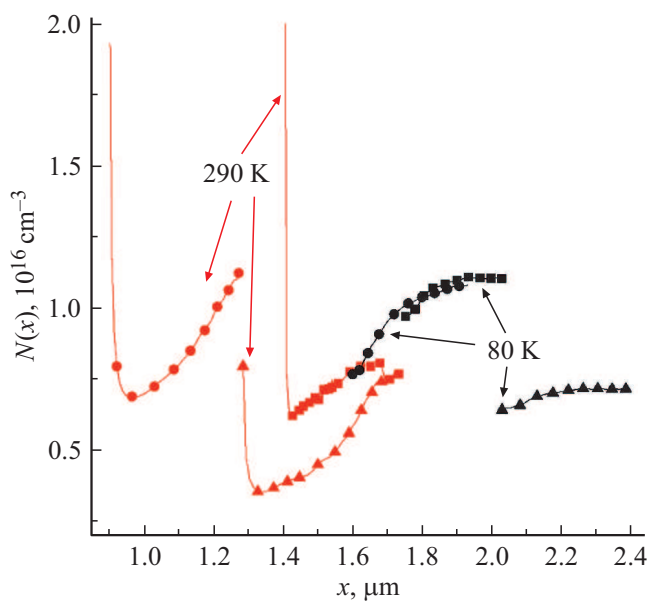
The $C-U$-characteristics of the samples after PLA, measured at 290 and 80 K, are shown in Fig. 9, a. Here, a non-monotonic capacitance dependence on reverse bias is only observed at 290 K. As a result of the PLA, the capacitance value of the samples at zero bias increased by an order of magnitude or more at $T = 290$ K and by a factor of nearly 10 at $T = 80$ K. With decreasing sample temperature, the barrier capacitance value decreases by 50 pF (at zero bias) for the structure after PLA at $W = 2$ J/cm^2 and by about 100 and 200 pF for the PLA mode with $W = 1.5$ and 2.5 J/cm^2, respectively. The highest barrier capacitance value is recorded for a post-PLA structure at $W = 2.5$ J/cm^2.

For the structure formed after PLA with $W = 2$ J/cm^2 (Fig. 9, b) compared to the sample without PLA, a significant decrease in SCR width ($\sim 1.4\,\mu$m at $T = 290$ K and zero bias) as well as an increase in hole concentration is observed. At $T_{reg} = 80$ K, the hole concentration is $\sim 1.5 \cdot 10^{16}$ cm^{-3}. At room temperature, the N value varies from $3 \cdot 10^{16}$ cm^{-3} (at zero bias) to $6 \cdot 10^{15}$ cm^{-3}, which is about an order of magnitude greater than the data from the Irwin curve for p-type silicon with $\rho = 10\Omega \cdot$ cm. It should be noted the higher value of the concentration of mobile carriers at nitrogen temperatures compared to the case for $T_{reg} = 290$ K.

After PLA at $W = 1.5$ J/cm^2, the structure is characterized by a lower concentration of mobile holes at both

Table 3. Photovoltaic efficiency of structures at $U_{rev} = -0.2$ V and $T = 290$ K, measured before and after heat treatment (400°C, 10 min)

Range illumination	Density of PLA energy, J/cm^2	I_L/I_D, a. u. before heat	I_L/I_D, a. u. after treatment
Full range	1.5	2.7	8.3
	2	6.8	10.2
	2.5	4.3	10.9
IR	1.5	1.3	1.5
	2	1.9	1.8
	2.5	1.3	1.4

Figure 9. Charge carrier concentration distributions $N(x)$ calculated from $C-U$-characteristics of Te-implanted silicon after laser pulse annealing with $W = 1.5$ J/cm^2 (▲), $W = 2$ J/cm^2 (■) and $W = 2.5$ J/cm^2 (●), measured at $T_{reg} = 290$ and 80 K.

measurement temperatures than for the sample after PLA at $W = 2$ J/cm^2. The SCR width at zero offset is also less than the previous sample at $T_{reg} = 290$ K and greater at $T_{reg} = 80$ K. To a certain extent, these results are consistent with the fact that the sample in question underwent less intensive PLA than the previous one. This refers to the concentration of mobile holes and the SCR width at low temperatures.

For a structure subjected to PLA with $W = 2.5$ J/cm^2, the dependence $N(x)$ has a non-monotonic form (Fig. 9). The concentration of mobile holes at $T_{reg} = 290$ K is greater than that of the previous two samples, and at $T_{reg} = 80$ K the same as that of the sample after PLA with $W = 2$ J/cm^2. The SCR width at zero offset is also, compared to the previous two systems, smaller. When a reverse voltage is applied to the diode, the free charge carriers are displaced

from the regions adjacent to the $p-n$-transition: the space-charge region becomes wider. The characteristics of the formed $p-n$-junctions, such as carrier concentration, barrier height, determine the SCR width.

The width of the SCR V measured for structures after PLA is described quite well by the expression [34] for a flat capacitor,

$$V = \frac{\varepsilon\varepsilon_0 \cdot S}{C}\left[\frac{2\varepsilon\varepsilon_0(U_{pn} + U)}{eN}\right]^{1/2}, \qquad (2)$$

where $\varepsilon = 12.5$ — dielectric constant of silicon, ε_0 — dielectric constant of vacuum, $\varepsilon_0 = 8.85 \cdot 10^{-12}$ F/m, S — area of top electrode of test structure (in our case $S = 4.121$ mm^2), U_{pn} is approximately equal to the band gap width of silicon expressed in volts (1.12 V), U — reverse bias voltage, N — concentration of mobile carriers in the less doped region. For the systems in question, after PLA $V = \dfrac{456\,\mu m \cdot pF}{C(pF)}$.

2.4. DLTS spectroscopy of samples

The emission activation energy and charge carrier capture cross sections were determined by non-stationary capacitive deep level transient spectroscopy (DLTS) [35]. The duration of the trap filling pulse was 10^{-2} s and the offset voltage value U_{biad} from -3 to -16 V. The spectra were measured in the temperature range $80-300$ K in the trap filling mode with the main charge carriers. Filling voltage $U_{occ} = 0$ V, emission velocity window $e = 19\,s^{-1}$.

Fig. 10 shows the DLTS spectra for all four systems discussed. For the H1−H3 traps, the parameters, activation energy and capture cross-section were determined. Trap H1 corresponds to a deep level in the Si band gap $E_V + 0.25$ eV and capture cross-section $\sigma = 2.5 \cdot 10^{-12}$ cm^{-2}; H2 — $E_V + 0.24$ eV and capture cross section $\sigma = 6.7 \cdot 10^{-15}$ cm^{-2} and H3 — $E_V + 0.34$ eV and capture cross section $\sigma = 1.8 \cdot 10^{-15}$ cm^{-2}. The very large carrier capture cross-section of trap H1 is noteworthy. These values correspond to shallow dopanrs.

The most intense H3 peak in the DLTS spectrum is most likely due to the presence of an impurity subzone in the
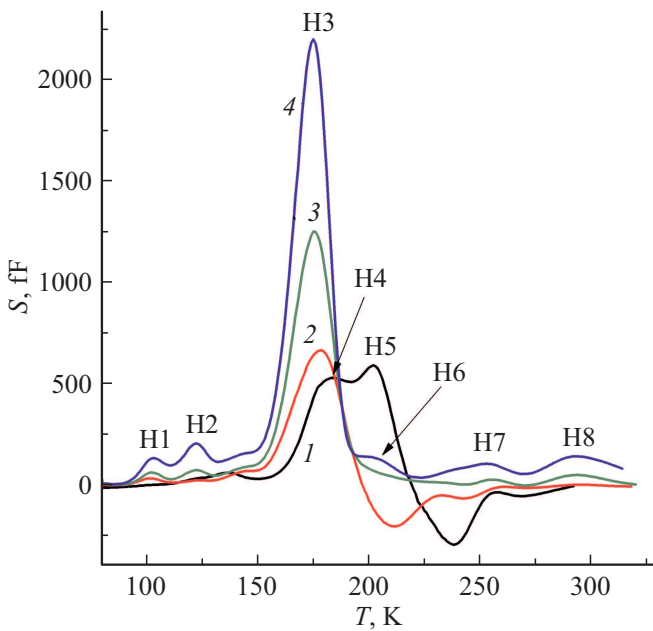
Figure 10. DLTS spectra of Te-implanted silicon before and after laser annealing, measured in trap filling mode with main charge carriers: *1* — without annealing; *2* — $W = 1.5\,\text{J/cm}^2$; *3* $W = 2\,\text{J/cm}^2$; *4* — $W = 2.5\,\text{J/cm}^2$.

band gap of silicon. For the tellurium doping level of silicon discussed above $(2.2-3.6 \cdot 10^{20}\,\text{cm}^{-3})$, this subzone can be located at a distance $\sim 0.3-0.5\,\text{eV}$ from the valence band. Clarification the nature of the other recorded peaks in the spectrum requires further research beyond the scope of this paper.

Conclusion

By implanting Te ions with $200\,\text{keV}$ energy at a fluence of $1 \cdot 10^{16}\,\text{cm}^{-2}$ followed by nanosecond laser annealing at energy density in pulse $1.5-2.5\,\text{Jcm}^2$, silicon layers hyperdoped with tellurium to concentration $(3-5) \cdot 10^{20}\,\text{cm}^{-3}$ were obtained. According to the RBS data, the embedded impurity is almost uniformly distributed in the implanted layer at a depth from the surface to $190\,\text{nm}$. In this case $70-90\%$ of the introduced impurity is in a substitution position in the silicon lattice.

In silicon hyper-saturated with tellurium there is an effective absorption of photons with energies less than the bandgap of silicon, i.e. in the wavelength range $\lambda > 1100\,\text{nm}$, up to the limiting measured $\lambda = 2500\,\text{nm}$. This process is caused by the formation of an impurity subzone in the band gap of silicon. This increases the absorption coefficient from $34-35\%$ at $\lambda = 1180\,\text{nm}$ to $55-65\%$ at $\lambda = 2500\,\text{nm}$. This is caused by good recrystallisation of the implanted silicon layer due to laser annealing and introduction of $70-90\%$ impurity into the substitution position in the silicon crystal lattice.

The influence of PLA and subsequent low-temperature annealing ($400°\text{C}$, $15\,\text{min}$) on their photosensitivity in both visible and near-infrared ranges was determined on the test photodetector structures. For the first time the photosensitivity of tellurium-doped amorphous Si layers in the IR region after the specified low-temperature annealing was found.

A number of recommendations are given to optimize the design of the device structure and the process conditions of their manufacture in order to significantly increase the collection efficiency of the light-generated current carriers. In this case, the structures created would be of interest both as photodetectors in the IR wavelength range and in the manufacture of efficient solar cells in silicon and with silicon technology.

Conflict of interest

The authors declare that they have no conflict of interest.

References

[1] R. Soref. Nat. Photonics, **9**, 358 (2015).
DOI: 10.1038/nphoton.2015.87

[2] X. Liu, B. Kuyken, G. Roelkens, R. Baets, R.M. Osgood Jr, W.M.J. Green. Nat. Photonics, **6**, 667 (2012).
DOI: 10.1038/nphoton.2012.221

[3] J.J. Ackert, D.J. Thompson, L. Shen, A.C. Peacock, P.E. Jessop, G.T. Reed, G.Z. Mashanovich, A.P. Knights. Nat. Photonics, **9**, 393 (2015). DOI: 10.1038/nphoton.2015.81

[4] P. Chaisakul, D. Marris-Morini, G. Isella, D. Chrastina, X. Le Roux, S. Edmond, E. Cassan, J-R. Coudevylle, L. Vivien. Appl. Phys. Lett., **98**, 131112 (2011).
DOI: 10.1063/1.3574539

[5] M. Casalino, G. Coppola, M. Iodice, I. Rendina, L. Sirleto. Sensors, **10**, 10571 (2010). DOI: 10.3390/s101210571

[6] J. Bradley, P. Jessop, A. Knights. Appl. Phys. Lett., **86**, 241103 (2005). DOI: 10.1063/1.1947379

[7] J. Doylend, P. Jessop, A. Knights. Opt. Express, **18**, 14671 (2010). DOI: 10.1364/OE.18.014671

[8] A. Rogalski. Prog. Quantum. Electron, **27**, 59 (2003).
DOI: 10.1016/S0079-6727(02)00024-1

[9] N. Sclar. Prog. Quantum. Electron, **9**, 149 (1984).
DOI: 10.1016/0079-6727(84)90001-6

[10] C.B. Simmons, A.J. Akey. J.P. Mailoa, D. Recht, M.J. Aziz, T. Bounassisi. Adv. Fun Mater., **24**, 2852 (2014).
DOI: 10.1002/adfm.201303820

[11] X. Qiu, Z. Wang, X. Hou, X. Yu, D. Yang. Photonics Res., **7**, 351 (2019). DOI: 10.1364/PRJ.7.000351

[15] E. Garcia-Hemme, R. Garcia-Hernansanz, J. Olea, D. Pastor. A. del Prado, I. Mártil, G. Gonzáles-Diaz. Appl. Phys. Lett., **103**, 032101 (2013). DOI: 10.1063/1.4813823

[13] H. Vydyanath, J. Lorenzo, F. Kröger. J. Appl. Phys., **49**, 5928 (1978). DOI: 10.1063/1.324560

[14] M.T. Winkler, D. Recht, M.J. Sher, A.J. Said, E. Mazur, M.J. Aziz. Phys. Rev. Lett., **106**, 178701 (2011).
DOI: 10.1103/PhysRevLett.106.178701

[15] H. Mehrer. *Diffusion in Solids: Fundamentals, Methdos, Material, Diffusion-Controlled Processes* (Springer Science and Business Media, NY., 2007), v. 155.

[16] I. Umezu, J.M. Warrender, S. Charnvanichborikarn, A. Kohno, J.S. Williams, M. Tabbal, D.G. Papazoglou, Xi-Ch. Zhang, M.J. Aziz. J. Appl. Phys., **113**, 213501 (2013). DOI: 10.1063/1.4804935

[17] E. Schibli, A.G. Milnes. Mater. Sci. Engineer., **2**, 173 (1967). DOI: 10.1016/0025-5416(67)90056-0

[18] F.F. Komarov, G. Ivlev, G. Zayats, A. Komarov, N. Nechaev, I. Parkhomenko, L. Vlasukova, E. Wendler, S. Miskiewicz. Acta Phys. Polonica, **A136**, 254 (2019). DOI: 10.12693/APhysPolA.136.254

[19] F.F. Komarov, N. Nechaev, G. Ivlev, L. Vlasukova, I. Parkhomenko, E. Wendler, I.A. Romanov, Y. Berencén, V.V. Pilko, D.V. Zhigulin, A.F. Komarov. Vacuum, **178**, 109434 (2020). DOI: 10.1016/j.vacuum.2020.109434

[20] Y. Berencén, S. Prucnal, F. Liu, I. Scorupa, R. Hübner. Scientific Reports, **7**, 43688 (2017). DOI: 10.1038/srep43688

[21] M. Mayer, SIMNRA User's Guide (Max-Planck-Institut fur Plasmaphysik, Garching, 1997)

[22] D.V. Lang. Appl. Phys., **45**, 3023 (1974). DOI: 10.1063/1.1663719

[23] A.F. Komarov, F.F. Komarov, P. Żukowski, C. Karwat, A.L. Shukan. Nukleonika, **44**, 363 (1999).

[24] L.C. Feldman, W. Mayer, S.T. Picraux. Materials Analysis by Ion Channeling: Submicron Crystallography (Elsevier, NY., 1982).

[25] F.F. Komarov, A.P. Novikov, V.S. Solovev, S.Yu. Shiryaev. *Structure Defects in Ion-Introduced Silicon* (Universitetskoe, Minsk, 1990)

[26] V.E. Borisenko. *Solid-phase processes in semiconductors at pulse heating* (Navuka i tekhnika, Minsk, 1992)

[27] W. Wesch, E. Glaser, G. Götz, H. Karge, R. Proger. Phys. Stat. Sol., **65**, 225 (1981), DOI: 10.1002/pssa.2210650126

[28] R. Shaub, G. Pensl, M. Schulz, C. Holm. Appl. Phys., **A34**, 215 (1984). DOI: 10.1007/BF00616575.

[29] N.F. Mott. Contemp. Phys., **14**, 401 (1973). DOI: 10.1080/00107517308210764

[30] M. Wang, A. Debernardi, Y. Berencén, R. Heller, C. Xu, Y. Yuan, Y. Xie, R. Böttger, L. Rebohle, W. Skorupa, M. Helm, S. Prucnal, Sh. Zhou. Phys. Rev. Appl., **11**, 054039 (2019). DOI: 10.1103/PhysRevApplied.11.054039

[31] E.F. Schubert. *Doping III−V Semiconductors* (Cambridge University Press, Cambridge, 1993)

[32] K. Sánchez, I. Aguilera, P. Palacios, P. Wahnón. Phys. Rev., **B82**, 165201 (2010). DOI:10.1103/Phys.RevB.82.165201

[33] N.A. Poklonsky, A.I. Kovalev. Instruments and Methods of Measurement, **9** (2), 130 (2018).

[34] M.E. Levinstein, G.S. Simin. *Barriers from Crystal to Integrated Circuit* (Nauka, M., 1987)

[35] D.V. Lang. J. Appl. Phys., **45** (2), 3023 (1974). DOI: 10.1063/1.1663719